

Article

# Study on the Optimal Design of a Shark-like Shape AUV Based on the CFD Method

Yu Lu <sup>1</sup>, Jianping Yuan <sup>1</sup>, Qiaorui Si <sup>1,\*</sup> , Peifeng Ji <sup>2</sup>, Ding Tian <sup>1</sup> and Jinfeng Liu <sup>1</sup>

<sup>1</sup> National Research Center of Pumps, Jiangsu University, Zhenjiang 212013, China; luyuujs@163.com (Y.L.)

<sup>2</sup> Key Laboratory of Noise and Vibration Research, Institute of Acoustics, Chinese Academy of Sciences, Beijing 100190, China

\* Correspondence: siqiaorui@ujs.edu.cn

**Abstract:** In previous AUV designs, the thrusters were often placed outside the vehicle, resulting in their performance being significantly influenced by the shape of the vehicle. Additionally, this placement also leads to the generation of strong radiated noise that propagates in all directions, making noise reduction challenging. Taking inspiration from the shape of sharks, this paper proposes a slender, shark-inspired AUV. The model features a continuous passageway in the middle where a pump-jet thruster is installed to provide propulsion. The walls of the passageway are then covered with sound-absorbing materials to reduce radiated noise. To address the problem of low design efficiency caused by multiple design parameters, a multi-objective optimization method is proposed to optimize the shape of the AUV. The performance targets of speed, displacement, and energy consumption are determined as objective functions, and a multi-island genetic algorithm is used as the optimization algorithm to build the multi-objective optimization process. An automated optimization platform was then developed which integrates parametric modeling, mesh partitioning, the CFD calculation, and the optimized design. To enhance the efficiency of optimization, a surrogate model was developed to approximate the CFD calculation. Using the optimal Latin hypercube method, experimental factors were designed, and a surrogate model was constructed based on the radial basis function approach. Following optimization, the resistance was reduced by 9.1%, while the displacement volume was increased by 10.7% and energy consumption was decreased by 6.3%. By analyzing the velocity and entropy production distribution of the AUV, the effectiveness of the optimization method was verified.



**Citation:** Lu, Y.; Yuan, J.; Si, Q.; Ji, P.; Tian, D.; Liu, J. Study on the Optimal Design of a Shark-like Shape AUV Based on the CFD Method. *J. Mar. Sci. Eng.* **2023**, *11*, 1869. <https://doi.org/10.3390/jmse11101869>

Academic Editor: Diego Villa

Received: 10 August 2023

Revised: 11 September 2023

Accepted: 21 September 2023

Published: 26 September 2023



**Copyright:** © 2023 by the authors. Licensee MDPI, Basel, Switzerland. This article is an open access article distributed under the terms and conditions of the Creative Commons Attribution (CC BY) license (<https://creativecommons.org/licenses/by/4.0/>).

**Keywords:** underwater vehicle; bionic design; CFD simulation; multi-objective optimization

## 1. Introduction

As an important tool to accomplish various underwater tasks, autonomous underwater vehicles (AUVs) are widely used in military and scientific fields. Low noise and high endurance are necessities for AUVs to accomplish their intended missions. In terms of safety, high-intensity noise will affect the operation of the equipment of the navigation hull, and in the military field, the presence of noise will directly affect the concealment of the hull and seriously reduce its survivability. In the design of AUVs, endurance is one of the primary considerations. Resistance is the main cause of energy consumption and reduced sailing speed, making reducing the resistance of the hull the most intuitive and effective way to reduce energy consumption and improve endurance. To decrease the resistance of the hull, automatic optimization design methods have been widely used in AUV design. When designing AUVs, underwater organisms provide new ideas. Through hundreds of millions of years of evolution, aquatic organisms have formed unique shapes and movement characteristics. By imitating the shape, surface texture, swimming style, or movement of aquatic organisms, the performance of AUVs can be effectively improved. This biomimetic design method has been widely applied to hull shape, propeller design

optimization, and other aspects. Therefore, combining natural design ideas with artificial intelligence can bring more possibilities for future AUV design.

The design of the craft usually considers hydrodynamic performance, range, and stability. Traditional optimization methods are generally carried out in a series-by-series way. In sophisticated design workflows, there is a complex coupling between disciplines and the whole system does not consist of a simple addition or combination of subsystems. Therefore, optimization methods that take into account the coupling between systems and are able to integrate the interactions between the various subsystems are crucial. For example, Zhao et al. [1] employed the reference vector-guided evolutionary algorithm (RVEA) to select the appropriate influential factors and combined surrogate models with multi-objective optimization algorithms to address computationally expensive multi-objective problems. Li et al. [2] divided the AUV system into five sub-disciplines for optimization design, with the AUV mass and payload as objective functions, and used the MOGA algorithm to obtain the PATERO solution set. Zhang et al. [3] used collaborative subspace optimization (CSSO) for the structural design of the vehicle, and the performance of the optimized model was significantly improved. Wu et al. [4] proposed a hybrid polynomial-based optimization method to establish Pareto bounds, with the hybrid polynomial consisting of power functions and trigonometric functions.

Suitable optimization methods provide clear approaches to the optimization of underwater navigational vehicles; however, the selection of optimization algorithms is also one of the issues that need to be addressed. Optimization algorithms can be divided into two categories according to the structure of the algorithm. The first category is gradient optimization algorithms, with the method of feasible directions (MFD), the method of single-level inequality constraints optimization (MOSI), and sequential quadratic programming (SQP) being the most commonly used. The second category is the global optimization algorithm, including the multiple island genetic algorithm (MIGA), simulated annealing algorithm (SA), and particle swarm optimization (PSO). These optimization methods can obtain the global optimal solution but converge more slowly than gradient optimization algorithms. In practical engineering problems, the objective function may exhibit multiple peaks and discontinuities, making it more suitable to employ global optimization algorithms to address such issues (Luo et al. [5]). Bidoki [6] used a particle swarm optimization algorithm to optimize underwater vehicles. Tian et al. [7] combined back propagation neural networks (BPNN) and genetic algorithms (GA) to investigate two underwater vehicle formation layout strategies. Yan et al. [8] proposed a whale algorithm based on perception, decision-making, and control systems to address the optimal path-planning problem for AUVs during navigation. The objective of their approach was to enable AUVs to efficiently avoid hazardous areas while minimizing energy consumption and completing a task in the shortest possible time.

Another problem that also needs to be taken into account is how to obtain accurate hydrodynamic performance of the model. Many researchers use CFD numerical simulations to evaluate the hydrodynamic performance of AUVs (Fuglestad et al. [9], Inoue et al. [10], and Safari et al. [11]). Jin et al. [12] designed the fairing section of an autonomous remotely operated vehicle (ARV) based on simulation results while Sener et al. [13] studied the effect of changes in the head shape of the model on the overall flow characteristics.

Optimization problems often involve a large number of repetitive calculation processes. Integrating the CFD calculation module directly into the optimization process can significantly reduce efficiency. To improve optimization efficiency, researchers have proposed using surrogate models to replace the CFD module's calculation tasks. Surrogate models are widely used in optimizing designs in fields such as aviation, vehicles, and ships. Jouhaud et al. [14] optimized the shape parameters of a wing using the optimal interpolation method based on the Kriging model. Luo et al. [15] employed the radial basis function method to construct a dynamic surrogate model and optimized the hull form of an AUV using this optimization scheme. Hu et al. [16] applied the self-adaptive surrogate ensemble model to the design of AUVs.

In recent years, researchers have applied bionics to the design of underwater vehicles. Their inspiration has come from many marine creatures for different design objectives, such as drag reduction and maneuverability. For example, Ardakani et al. [17] established a V-shaped groove rib theory with a high Reynolds number based on the surface groove of shark scales to guide the parameter optimization of surface texture and realize drag reduction in underwater vehicles. Wang et al. [18] designed a jet-propelled bionic scallop that imitates the opening and closing of a scallop shell to achieve forward motion. Xu et al. [19] studied the bionic swim bladder system of underwater animals and found that it can enhance the maneuverability of robots.

Taking into account speed, endurance, and displacement, this paper applies a multi-objective genetic optimization algorithm to the shape optimization of the bio-inspired shark-like AUV proposed by the author. In order to reduce noise, the biologically-inspired AUV proposed in this paper is equipped with a hollow channel inside its body, and the propulsion device is built inside the boat to facilitate the laying of sound-absorbing and vibration-reducing materials to ensure the AUV's stealthiness. The CFD method is used to compute the resistance of the AUV. In order to verify the accuracy, the resistance simulation results of the DAPRA SUBOFF model are compared with publicly available experimental data first. In Section 3, we describe the parameterization of the proposed shark-inspired AUV model and determine its influencing factors. Due to the long response time of the CFD method and considering efficiency and design economics, a surrogate model based on radial basis functions (RBF) is used. Before establishing the surrogate model, the optimal Latin hypercube method is used to determine the required experimental matrix, and Isight is used to build the Fluent automatic calculation platform to obtain the sample point set to construct the database. In Section 4, the automatic optimization process integrating 3D modeling, mesh pre-processing, CFD result analysis, and the optimization module on the Isight platform will be introduced. Finally, the flow field information before and after model optimization will be compared and analyzed to prove the effectiveness of the optimization.

## 2. CFD Method

An efficient and accurate method to analyze the hydrodynamic performance of an AUV is the CFD method. This method has been a research hotspot in the fields of ship and ocean engineering and has achieved remarkable research results. In this study, FLUENT software was first used to perform numerical calculations on the bare hull of a DAPRA SUBOFF. To validate the accuracy of the CFD method, the detailed experimental values were used for simulations. The external shape of the DAPRA SUBOFF model is shown in Figure 1. The model has a length of  $L_s = 4.356$  m and a maximum diameter of  $D_s = 0.508$  m.

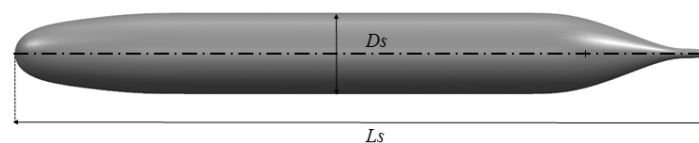


**Figure 1.** DARPA SUBOFF.

### 2.1. Governing Equations

In the field of turbulence research, numerical simulation methods mainly include direct numerical simulation (DNS), Reynolds-averaged Navier–Stokes simulation (RANS), and large eddy simulation (LES). The DNS method can theoretically obtain exact solutions, but it requires extremely high computational resources and cannot be used for engineering projects. On the other hand, the prerequisite for using the LES (large eddy simulation) method is the requirement of a high-precision grid and a significant number of computational resources. Considering both the computational accuracy and cost, the RANS equation is used as the governing equation. By performing time averaging on the momen-

tum conservation equation and continuity equation, the RANS equation can be represented by the following form:

$$\frac{\partial u_i}{\partial x_i} = 0 \tag{1}$$

$$\rho \frac{\partial u_i}{\partial t} + \rho u_j \frac{\partial u_i}{\partial x_j} = -\frac{\partial p}{\partial x_i} + u_j \frac{\partial}{\partial x_j} \left( \frac{\partial u_i}{\partial x_j} - \overline{\rho u'_i u'_j} \right) + S_i \tag{2}$$

where  $u_i$  and  $u_j$  are velocity components and  $\overline{\rho u'_i u'_j}$  is the Reynolds stress.

In addition, the RANS equation requires the use of an additional turbulence model for closure. In this study, the SST  $k-\omega$  model is chosen as the turbulence model. According to experimental evidence from researchers, it has been proven that the SST  $k-\omega$  model accurately predicts the resistance of a ship (Pena et al. [20], Huang et al. [21]). Won et al. [22] successfully simulated the propulsion process of a ship using the SST  $k-\omega$  model, and the simulation results were consistent with experimental data. The  $k$  and  $\omega$  equations of the SST  $k-\omega$  turbulence model are defined as follows.

$$\frac{\partial(\rho k)}{\partial t} + \frac{\partial(\rho k u_i)}{\partial x_i} = \frac{\partial}{\partial x_j} \left[ \left( \mu + \frac{\mu_t}{\sigma_{k3}} \right) \frac{\partial k}{\partial x_j} \right] + P_k - \beta^* \rho k \omega \tag{3}$$

$$\begin{aligned} \frac{\partial(\rho \omega)}{\partial t} + \frac{\partial(\rho \omega u_i)}{\partial x_i} &= \frac{\partial}{\partial x_j} \left[ \left( \mu + \frac{\mu_t}{\sigma_{\omega 3}} \right) \frac{\partial \omega}{\partial x_j} \right] + \alpha_3 \frac{\omega}{k} P_k \\ &- \beta_3 \rho \omega^2 + 2(1 - F_1) \rho \frac{1}{\omega \sigma_{\omega 2}} \frac{\partial k}{\partial x_j} \frac{\partial \omega}{\partial x_j} \end{aligned} \tag{4}$$

where  $\mu_t$  is the turbulent viscosity and  $P_k$  represents the turbulence production term caused by the viscous forces:

$$\mu_t = \rho \frac{\alpha_1 k}{\max(a_1 \omega, S F_2)} \tag{5}$$

$$P_k = \mu_t \left( \frac{\partial u_i}{\partial x_j} + \frac{\partial u_j}{\partial x_i} \right) \frac{\partial u_i}{\partial x_i} - \frac{2}{3} \frac{\partial u_k}{\partial x_k} \left( 3 \mu_t \frac{\partial u_k}{\partial x_k} + \rho k \right) \tag{6}$$

### 2.2. Computational Domain and Meshing

It is crucial to choose a suitable computational domain for the model (Luo et al. [15] and Hu et al. [23]). Figure 2 shows the computational domain and boundary conditions of the model. The distance from the inlet of the computational domain to the top of the head of the hull is  $1L_s$ , and the distance from the afterbody cap to the outlet of the computational domain is  $2L_s$ . The fluid domain is set as a column-shaped area with a diameter of  $2L_s$ . The inlet boundary condition is set as the velocity inlet and the outlet boundary is set as the pressure outlet. The value of the inflow velocity corresponds to the speed at which the body travels when moving at a constant velocity. In this validation case, the speed of the DARPA SUBOFF is set to 3.0455 m/s, and the pressure value at the outlet boundary is set to 1 atm.

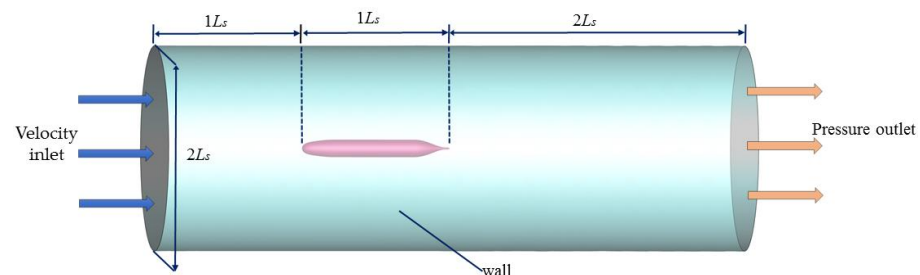
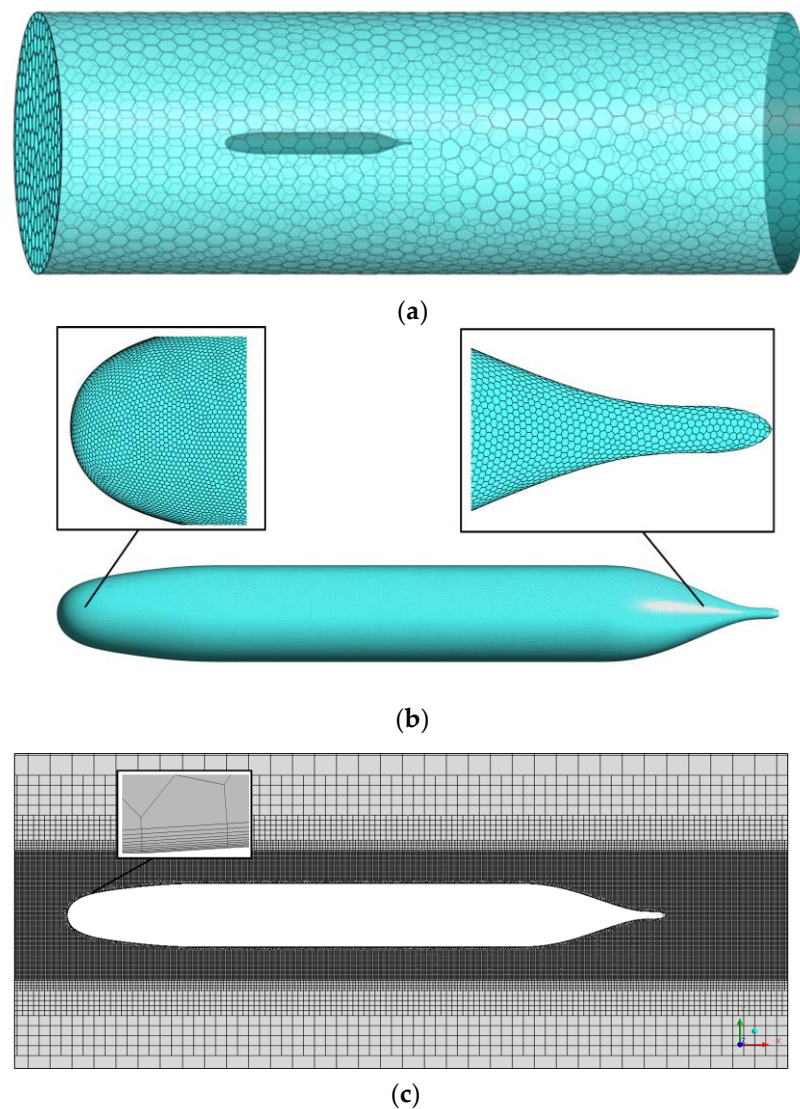


Figure 2. Calculation domain and boundary condition settings.

In order to achieve automatic optimization, an unstructured grid division is adopted in this study. Following the findings of Hu et al. [16], prism layer elements with a growth rate of 1.1 are added near the wall surface to maintain a non-dimensional wall distance ( $y^+$ ) below 5. To effectively manage the number of grid cells, the mesh is generated using minimum grid sizes of 2.18 mm, 4.36 mm, 6.54 mm, 8.72 mm, and 10.9 mm. Figure 3 illustrates the grid of the entire computational domain, including the surface grid of the submarine. The grid size gradually increases towards the outer wall of the cylindrical fluid domain. By utilizing an octree grid generation algorithm, the maximum grid size is automatically set to 32 times the minimum size. Figure 3b provides an enlarged view of the submarine's head and tail.



**Figure 3.** Details of the computation mesh. (a) Computation mesh, (b) surface mesh, and (c) grid around the surface.

CFD simulations are performed on a workstation equipped with a 48-core INTEL(R) Xeon(R) Platinum 8174 CPU. The resistance for different schemes at a speed of 3.0455 m/s is shown in Table 1. As the number of grids increases, the resistance value gradually decreases. The difference in resistance values between Scheme 4 and Scheme 5 is only 0.4%, but the computation time of Scheme 5 is increased by 96% compared to Scheme 4. In order to ensure the accuracy of the CFD method, Scheme 4 is selected as the subsequent grid

partitioning strategy. It should be noted that the minimum size of Scheme 4 is 4.36 mm, which is approximately one-thousandth of the model length,  $L_s$ .

**Table 1.** Comparison of the drag values using different grid schemes.

Grid Scheme	Minimum Size (mm)	Number of Grids ( $10^4$ )	Computational Time (h)	Resistance (n)
1	10.9	152	1.2	92.86
2	8.72	283	2.1	91.41
3	6.54	422	3.8	90.93
4	4.36	875	5.3	90.61
5	2.18	1341	10.4	90.42

### 2.3. Verification

The fourth grid scheme was used for different speeds, and the comparison between the calculated values and the experimental values (Liu et al. [24]) is shown in Table 2. The results indicate that the error between the CFD simulated values and experimental values is within 5%, validating the reliability of the CFD method in simulating ship resistance.

**Table 2.** Comparison of CFD simulation and experimental values.

V (m/s)	CFD (N)	Experiment (n)	Error
3.0455	90.61	87.4	3.54%
5.1444	240.3	242.2	0.78%
6.0910	329.6	332.9	1.00%
7.1610	447.8	451.5	0.83%
8.2311	576.58	576.9	0.06%

## 3. Optimal Design Method

### 3.1. Original Model

In terms of shape, underwater vehicles can be primarily classified into glider-type, flat fish-shaped, multi-rotor, and cylindrical bodies [25]. Glider-type AUVs utilize net buoyancy and adjustments in attitude angle to generate propulsion. This design results in lower energy consumption and stronger endurance, although typically at lower speeds. The flat fish-shaped AUV’s exterior is advantageous in reducing vertical surface resistance and facilitates ascent and descent operations. However, it requires complex control systems and often necessitates the use of multiple thrusters and rudders in combination. Multi-rotor AUVs offer flexible maneuvering capabilities, but generally experience higher resistance, resulting in shorter endurance at higher speeds. The slender and rotating body design of the cylindrical AUV is widely utilized due to its low resistance, stable navigation, and ease of installation and manufacturing. However, in previous designs, the thrusters were often placed outside the vehicle, resulting in their performance being significantly influenced by the shape of the vehicle. Additionally, this placement also led to the generation of strong radiated noise that propagated in all directions, making noise reduction challenging [26]. Sharks have evolved naturally to effortlessly navigate in the deep sea, making their body shape a valuable reference for optimizing deep-sea vehicles. This paper proposes a shark-inspired AUV with a slender shape and built-in thrusters. The initial model is a shark-like AUV (Figure 4) featuring a continuous passageway with a pump-jet thruster installed inside to provide propulsion and reduce noise levels by employing sound-absorbing materials. In the figure, the black dashed line represents the direction of water flow, while the red dashed line shows the internal flow channels of the AUV. Among them,  $D_1 = D_2 = 300$  mm and  $D_3 = 250$  mm. Figure 5 shows the outer profile curve of the model. The preliminary design of the vehicle is divided into three sections: the forebody, the middle body, and the afterbody. The overall length  $L$  is 8 m. The water flows through the propulsion system and

is ejected at a certain speed from the nozzles to provide power; four wing-shaped devices are mounted to control the direction.

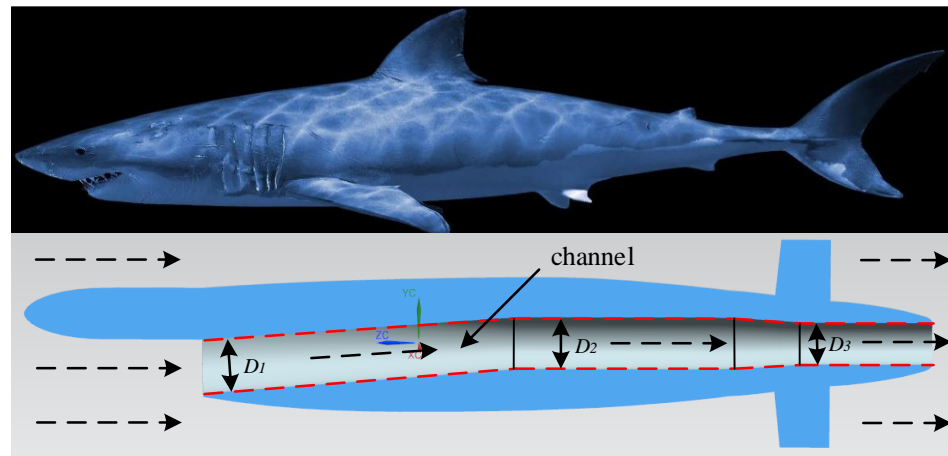


Figure 4. The proposed AUV.

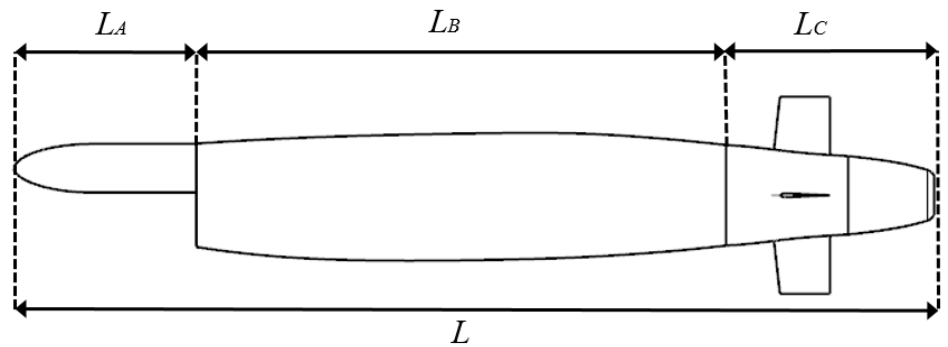


Figure 5. AUV modal.

To ensure the stability of the AUV during travel, the AUV’s hull features a revolved body shape at both its bow and stern. The Myring equation is used as a reference to describe the profile equations of the forebody and afterbody, which are represented by Equations (7) and (8), respectively. The parameters of the forebody are shown in Figure 6 and the parameters of the afterbody are shown in Figure 7.

$$r(x) = \frac{1}{2}d_1 \left[ 1 - \left( \frac{x-a}{a} \right)^2 \right]^{1/n} \tag{7}$$

$$r(x) = \frac{1}{2}d_2 - \left( \frac{3d_2}{2c^2} - \frac{\tan \theta}{c} \right) (x - L_A - L_B)^2 + \left( \frac{d_2}{c^3} - \frac{\tan \theta}{c^2} \right) (x - L_A - L_B)^3 \tag{8}$$

where  $d_1$  is the diameter of the forebody;  $d_2$  represents the maximum diameter of the afterbody; the symbols  $n$  and  $\theta$  are used to represent the degree of saturation for the afterbody and forebody shapes, respectively, with higher values indicating a fuller shape; and  $x$  is the distance from the point on the horizontal axis to the head of the AUV.

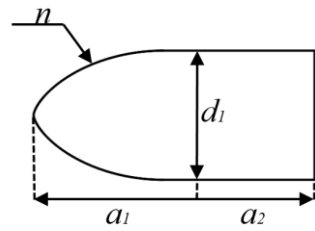


Figure 6. Forebody lines.

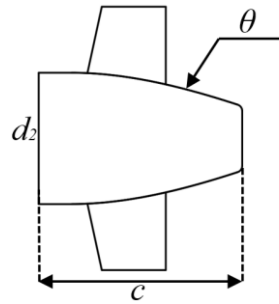


Figure 7. Afterbody lines.

In order to establish the equation of the AUV’s shape line, the coordinate origin is set at the center point of the left end section, and the coordinates of the important points ( $L_x$  and  $B_x$ ) and shape angles ( $\alpha_1$ ,  $\beta_1$ ,  $\alpha_2$ , and  $\beta_2$ ) of the external shape are selected as design variables. Figure 8 shows the top and front views, where the characteristic points of the hull are represented in three-dimensional coordinates, and the angle of the key lines are represented in the two-dimensional projection view as vector angles (the angle between the arrow and the X-axis).

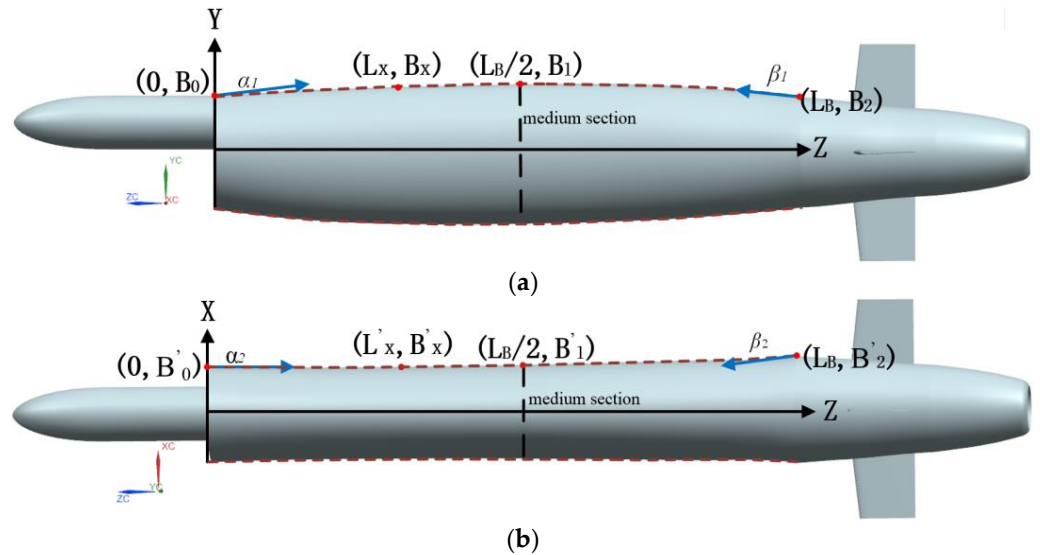


Figure 8. Definition of the parameters for the middle body. (a) Front view and (b) top view.

The critical contour lines of the AUV are defined through a two-dimensional projection based on a uniform  $n$ -th order B-spline curve. The two-dimensional projection function and its derivatives for these key contour lines are defined as follows:

$$S(u) = \sum_{j=0}^m P_j B_j^n(u) = (X(u), Y(u)) = \sum_{j=0}^m (X_j B_j^n(u), Y_j B_j^n(u)) \quad (9)$$

$$S'(u) = \sum_{j=0}^m P_j B_j^n(u) = (X(u), Y(u)) = \sum_{j=0}^m (X_j B_j^n(u), Y_j B_j^n(u)) \tag{10}$$

where  $P_j = (X_j, Y_j) (j = 0, 1, \dots, m), u \in [0, 1], B_j^n$  is the  $j$ th  $B$ -sample basis function. The basis function expressions are Equations (11) and (12). The 2nd and 3rd order  $B$ -sample basis functions with three and four control points and their derivatives derived from the Cox-de Boor formula are shown in Table 3.

$$B_j^0(u) = \begin{cases} 1 & (u \in [u_j, u_{j+1}]) \\ 0 & (u \notin [u_j, u_{j+1}]) \end{cases} \tag{11}$$

$$B_j^1(u) = \frac{u - u_j}{u_{j+1} - u_j} B_j^{n-1}(u) + \frac{u_{j+n+1} - u}{u_{j+n+1} - u_{j+1}} B_j^{n-1}(u) \tag{12}$$

**Table 3.** The 2nd and 3rd order  $B$ -sample basis functions and derivatives.

$j$	$B_j^2$	$B_j^3$	$B_j^2$	$B_j^2$
0	$(1 - u)^3$	$-3(1 - u)^2$	$(1 - u)^2$	$-2(1 - u)$
1	$3u(1 - u)^2$	$3(1 - u)^2 - 6u(1 - u)$	$2u(1 - u)$	$2 - 4u$
2	$3u^2(1 - u)$	$6u(1 - u) - 3u^2$	$u^2$	$2u$
3	$u^3$	$3u^2$	0	0

The 2D projection of the chord in the top view starts from the initial point  $S_0 (0, B_s)$ , passes through the transition point  $S_X (L_X, B_X)$ , and ends at the final point  $S_2 (L, 0)$ . The chord is a  $B$ -sample curve controlled by four points  $S_0, P_1 (X_{P1}, Y_{P1}), P_2 (X_{P2}, Y_{P2})$ , and  $S_2$ , as shown in Figure 9. The chord can be expressed by Equations (13) and (14). By using the constraint conditions, a system of equations can be formed to solve for the unknown variables. Similarly, the two-dimensional projection of the chord in the front view, from the start point through the transition point to the end point, is shown in Figure 10. The functions are represented by Equations (15) and (16).

$$s_p(u) = B_0^3(u)S_0 + B_1^3(u)P_1 + B_2^3(u)P_2 + B_3^3(u)S_2 \tag{13}$$

$$\begin{bmatrix} 0 & B_1^3(u^*) & 0 & B_2^3(u^*) \\ 0 & 0 & -\tan \alpha_1 & 1 \\ B_1^3(u^*) & 0 & B_2^3(u^*) & 0 \\ 0 & B_1^3(u^*) & 0 & B_2^3(u^*) \end{bmatrix} \begin{bmatrix} X_{P1} \\ Y_{P2} \\ X_{P1} \\ Y_{P2} \end{bmatrix} = \begin{bmatrix} -B_0^3(u^*) \\ -(\tan \alpha_1)L \\ L_X - B_3^3(u^*)L \\ B_X - B_0^3(u^*)B \end{bmatrix} \tag{14}$$

$$s'_p(u) = B_0^3(u)S'_0 + B_1^3(u)P'_1 + B_2^3(u)P'_2 + B_3^3(u)S'_2 \tag{15}$$

$$\begin{bmatrix} 0 & B_1^3(u^*) & 0 & B_2^3(u^*) \\ 0 & 0 & -\tan \alpha_2 & 1 \\ B_1^3(u^*) & 0 & B_2^3(u^*) & 0 \\ 0 & B_1^3(u^*) & 0 & B_2^3(u^*) \end{bmatrix} \begin{bmatrix} X_{P1}' \\ Y_{P2}' \\ X_{P1}' \\ Y_{P2}' \end{bmatrix} = \begin{bmatrix} -B_0^3(u^*) \\ -(\tan \alpha_2)L \\ L'_x - B_3^3(u^*)L \\ B'_x - B_0^3(u^*)B \end{bmatrix} \tag{16}$$

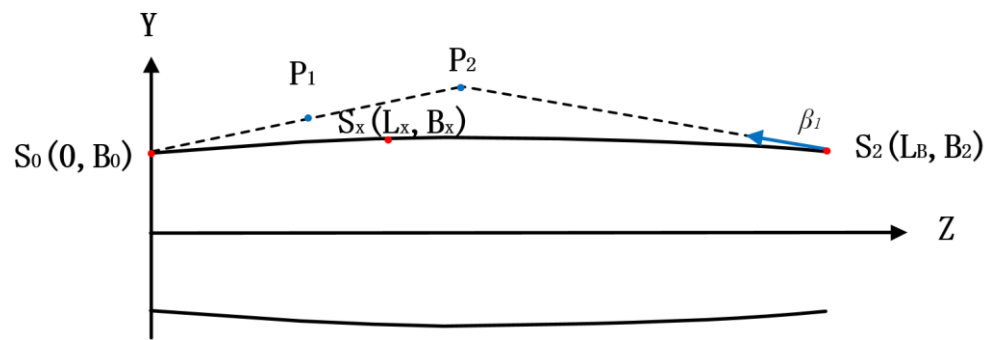


Figure 9. Two-dimensional projection of the chord line (front view).

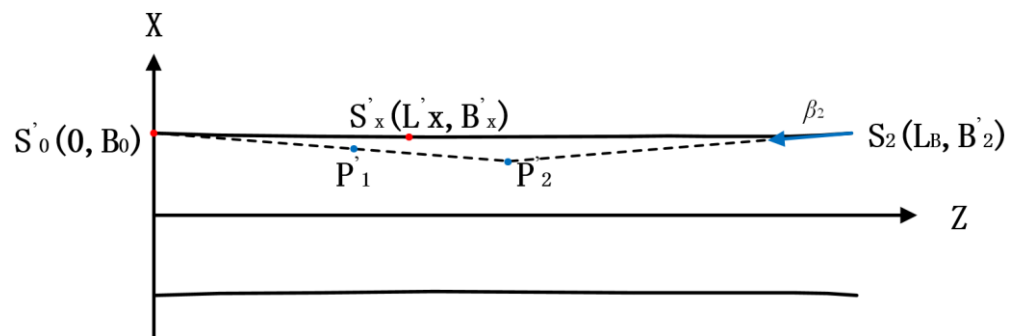


Figure 10. Two-dimensional projection of the chord line (top view).

### 3.2. Surrogate Model and Multi-Objective Optimization Method

#### 3.2.1. Overview of Multi-Objective Optimization Methods

The problem of multi-objective optimization is prevalent in all areas of reality and focuses on the simultaneous optimization of multiple numerical objectives in specific environments. In practice, there are limitations to achieving optimal solutions for each objective simultaneously. The subobjectives are commonly associated with each other and the optimization of a single objective often leads to a reduction in the performance of the other objectives. To solve this problem, it is necessary to coordinate various objectives, aiming to achieve the optimal solution for all sub-objectives as much as possible. The expression of multi-objective optimization problems can be described in the following mathematical form:

$$\min y = F(x) = (f_1(x), f_2(x), \dots, f_m(x)) \tag{17}$$

$$\text{subject to : } g_i(x) \leq 0, i = 1, 2, \dots, p, x \in D \tag{18}$$

where  $x \in D \subset R^n$  is the n-dimensional decision variable,  $x = (x_1, x_2, \dots, x_i)$ ,  $x_i$  denotes the  $i$ th decision variable,  $D$  denotes the solution range,  $f_i(x)$  is the  $i$ -th objective component of the objective function  $F(x)$ ,  $g_i(x) \leq 0$  ( $i = 1, 2, \dots, p$ ), and  $p$  denotes the number of constraints.

#### 3.2.2. Design of Experiment

Appropriate experimental design methods can ensure the good spatial accuracy of the test sample and obtain the highest possible test precision. Commonly used methods include orthogonal arrays, the full factorial design (FFD), the central composite design (CCD), the Latin hypercube design (LHD), and the optimal Latin hypercube design (OptLHD). Among these methods, the optimal Latin hypercube method has the lowest number of sample points and effective space-filling capability and also shows good balance, which is suitable for experimental designs with many impact factors. In this study, the OptLHD was used to reduce the size of the experiment.

In order to simplify the complexity of the system as well as to speed up the optimization, the lengths of the forebody and afterbody are set as constants, and the middle body is arranged symmetrically along the central axis (i.e.,  $\alpha_1 = \beta_1$  and  $\alpha_2 = \beta_2$ ). The main parameters affecting the shape of the navigating body include  $n$  and  $\theta$ , the angle ( $\alpha_1$ ) between the tangent line and the transverse axis at the starting point in the front view, the chord center coordinates ( $L_x, B_x$ ), the angle ( $\alpha_2$ ) between the tangent line and the transverse axis at the starting point in the top view, the chord center coordinates ( $L'_x, B'_x$ ), and the maximum diameters  $d_1$  and  $d_2$ . Subject to the constraints, the feasible domains for each parameter are summarized in Table 4.

**Table 4.** Ranges of optimization variables.

Parameter	Type	Range
$v$ (m/s)	Constant	3.0867
$L_A$ (mm)	Constant	1600
$L_C$ (mm)	Constant	1600
$d_1$ (mm)	Variable	(200, 500)
$d_2$ (mm)	Variable	(500, 650)
$n$	Variable	(0.6, 3.0)
$\theta$	Variable	(0.6, 3.0)
$L_x$ (mm)	Variable	(1990, 2010)
$B_x$ (mm)	Variable	(690, 710)
$\alpha_1$ (°)	Variable	(150, 170)
$L'_x$ (mm)	Variable	(1990, 2500)
$B'_x$ (mm)	Variable	(300, 350)
$\alpha_2$ (°)	Variable	(150, 170)

The number of samples for the experimental design should be appropriately chosen based on the size and complexity of the problem factors. According to Schmit et al. [27], the recommended number of experiments required to construct an experimental matrix using experimental design methods is  $((x + 1)(x + 2)/2 + 2x)$ , where  $x$  represents the number of factors. To improve the accuracy of the surrogate model, a total of 100 sample points were selected in this study. Table 5 displays the first ten sample point sets based on the Latin hypercube design. Based on the sample point set, a three-dimensional model with 10 parameter variables was generated and subsequently used for CFD resistance calculations to establish an approximation model.

**Table 5.** Latin hypercube design samples.

Sample	$d_1$	$d_2$	$n$	$\theta$	$L_x$	$B_x$	$\alpha_1$	$L'_x$	$B'_x$	$\alpha_2$
1	225.3	532.7	0.6	1	1990.0	697.2	155.6	1996.7	692.6	143.1
2	261.6	502.4	0.624	1	2006.4	708.5	168.5	1999.2	698.7	152.8
3	390.7	624.2	0.648	1	2006.9	692.1	154.1	2005.4	694.1	143.6
4	358.9	582.3	0.672	1.5	1996.2	705.4	159.2	2006.9	703.3	157.4
5	257.2	547.9	0.696	1.5	2008.0	692.6	167.4	1995.1	695.6	148.7
6	285.3	578.5	0.72	1.5	1994.6	706.4	158.7	1998.2	705.4	144.1
7	322.2	621.2	0.744	2	2002.3	703.3	152.6	2003.3	690.0	153.9
8	306.1	599.4	0.768	2	1992.6	693.6	166.4	1991.5	701.8	150.3
9	439.4	521.4	0.792	2	2009.5	707.4	161.3	2001.3	700.3	140.0
10	435.4	622.7	0.816	1	1993.6	697.7	163.3	2008.0	707.4	155.4

### 3.2.3. Surrogate Model

The choice of an accurate and reasonable agent model directly affects the efficiency and computational cost of optimization. Commonly used are the response surface model (RSM), Kriging, orthogonal polynomial, radial basis function (RBF), and random forest

model. In this study, the RBF model is used for an unknown function,  $f(x)$ , which can be expressed as Equation (19).

$$f(x) = \sum_{k=1}^m \lambda_i \varphi(\|x - x_k\|) \tag{19}$$

where  $x$  is the input variable;  $\lambda_i$  is the coefficient to be determined for the basis function;  $\|x - x_k\|$  is the Euclidean norm; and  $\varphi$  is the radial basis function. It can be expressed as

$$\varphi(\|x - x_k\|) = e^{-d^2\|x-x_k\|^2} \tag{20}$$

By using the RBF (radial basis function) model, it is possible to effectively replace multidimensional complex problems with one-dimensional problems, which have excellent approximation performance for higher-order non-linear functions (Wu [28]). If considered as a sum of weighted functions, the RBF model has weights that depend only on the number of samples and it is able to allow for the input of outliers, taking the drag ( $F_D$ ), volume  $V$ , and energy consumption ( $N_e$ ) as variables to establish the respective surrogate models. To verify the accuracy of the proxy model, the error accuracy was judged using a determinable coefficient of error  $R^2$  (21). The coefficient of determination of  $F_D$ ,  $V$ , and  $N_e$  are 0.982, 0.976, and 0.973, respectively.

$$R^2 = 1 - \frac{\sum_{i=1}^N (y_i - \tilde{y}_i)^2}{\sum_{i=1}^N (y_i - \bar{y}_i)^2} \tag{21}$$

#### 4. Shape Optimization of Underwater Vehicles Based on the Intelligent Optimization Algorithm

##### 4.1. Isight Multi-Objective Optimization Platform

Isight is a powerful computer-aided optimization (CAO) platform that provides a wide range of algorithms for design optimization. It can automatically run batch files to drive the simulation process and analyze the simulation values. The user can build a complete simulation and optimization platform using Isight. In the program, modeling is complete in UG, automatic meshing is carried out by ICEM, and the mesh file is then imported into Fluent for numerical simulation. The results of the numerical simulation are passed to the optimization component which then proceeds to the next simulation process until the optimization has been completed.

The genetic algorithm (GA) is a versatile global optimization algorithm that is inspired by the mechanism of genetic reproduction in biological evolution. In this study, the multi-island genetic algorithm (MIGA), a modification of the GA, which has better global optimization capabilities and computational efficiency, is applied. In the design of an AUV's exterior, the goal is to optimize the shape in order to achieve two objectives: increasing the payload capacity and minimizing resistance as much as possible. Considering the resistance, the volume of the hull, as well as the energy consumption, the objective function to be established is as follows:

Resistance:

$$\text{minimize} : \{F_D\} \tag{22}$$

Displacement volume:

$$\text{maximize} : \{V\} \tag{23}$$

where  $F_D$  represents the direct resistance of the hull;  $V$  represents the displacement volume of the hull, which can be obtained directly during the modeling process.

Referring to the mathematical description of the maximum range problem by Song et al. [29], the energy consumption can be represented as:

Energy consumption:

$$Minimize : \{N_e\} \tag{24}$$

$$S.t : \begin{aligned} &200 \text{ mm} \leq d_1 \leq 500 \text{ mm} \quad 500 \text{ mm} \leq d_2 \leq 650 \text{ mm} \quad 0.5 \leq n \leq 3.0 \quad 0.5 \leq \theta \leq 3.0 \\ &1990 \text{ mm} \leq L_x \leq 2500 \text{ mm} \quad 500 \text{ mm} \leq B_x \leq 550 \text{ mm} \quad 1990 \text{ mm} \leq L'_x \leq 2500 \text{ mm} \\ &300 \text{ mm} \leq B'_x \leq 350 \text{ mm} \quad 150 \leq \alpha_1 \leq 170 \quad 150 \leq \alpha_2 \leq 170 \end{aligned}$$

which can be expressed as:

$$N_e = \frac{\rho C_d A_T v^3}{2\eta_p} \tag{25}$$

where  $C_d$  is the hull resistance coefficient;  $A_T$  is the wetted surface area of the hull; and  $\eta_p$  is the propulsion efficiency and is set as a constant of 0.85.

Figure 11 is the schematic of the optimization platform and the optimization process. The optimization process consists of four parts: the RSM module, the displacement volume calculation module, the energy consumption calculation module, and the intelligent optimization module.

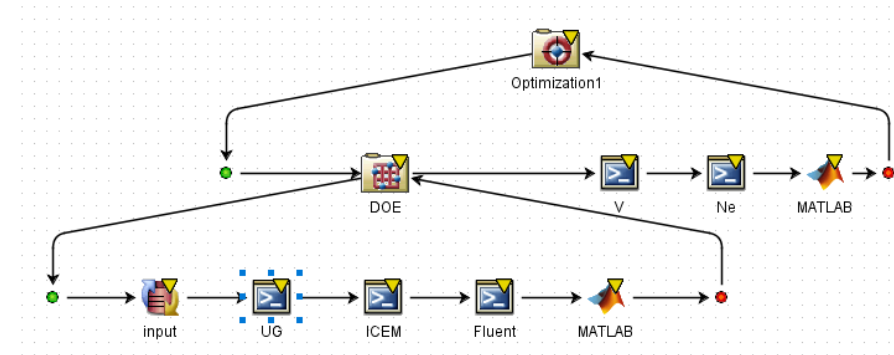


Figure 11. Isight optimization platform.

#### 4.2. Optimization Results

The grid partition strategy required for the CFD calculations is consistent with the approach described in Section 2.2. It involves utilizing the same minimum size and boundary layer settings to ensure that the non-dimensional distance near the wall is kept below 5. Table 6 shows the geometric parameters and results for the initial and optimized solutions for the AUV. At a speed of 3.0867 m/s, the resistance is reduced from 658 N to 598 N while the displacement volume is increased by 10.7% and the energy consumption is reduced by 6.3%.

Table 6. Optimization results for the AUV.

Parameters	$d_1$ (mm)	$d_2$ (mm)	$n$	$\theta$	$L_x$ (mm)	$B_x$ (mm)	$\alpha_1$	$L'_x$ (mm)	$B'_x$ (mm)	$\alpha_2$	$F_D$ (N)	$V$ (m <sup>3</sup> )	$N_e$ (N·m/s)
Initial scheme	300	825	1.0	3.0	2000	500	150	2000	300	150	658	2.219	3562
Optimized scheme	383	711	1.9	2.0	2405	524.5	165	2322	335.6	158	598	2.464	3237

Figure 12 shows the pressure distribution cloud maps at the head of the AUV for different values of  $n$ . As the value of  $n$  increases, the high-pressure area at the inlet of the AUV gradually expands. At  $n = 1.5$ , the pressure at the inlet section is at its maximum, while at  $n = 2$ , the high-pressure area at the inlet section sharply decreases. This indicates that, under this particular head shape ( $n = 2$ ), the streamlining of seawater becomes smoother after passing through the head.

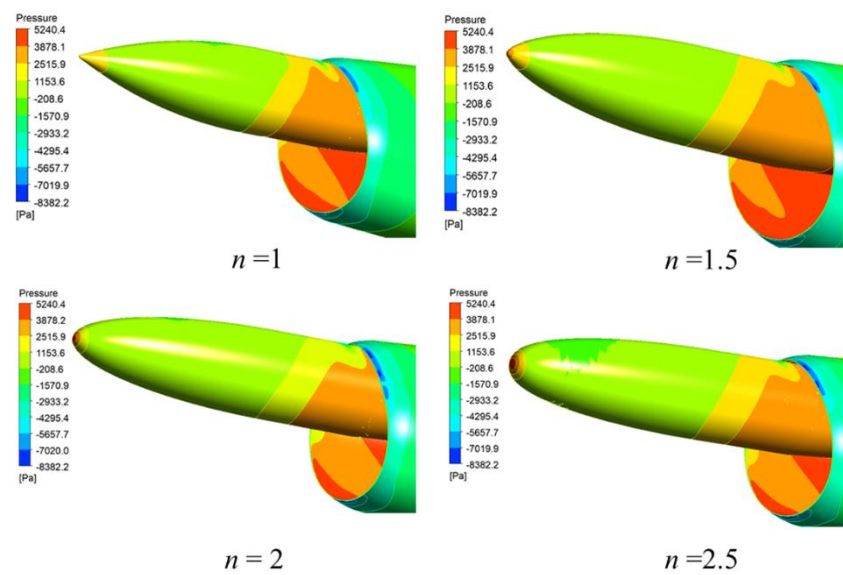


Figure 12. The pressure distribution at the forebody.

Figure 13 depicts the streamline distribution of the model’s mid-section, where the color of the streamlines corresponds to the magnitude of the velocity. In Figure 13a, a vortex is observed within the region enclosed by the red dashed line. In contrast, Figure 13b shows that, after optimization, the streamline distribution in that region of the model becomes more uniform, eliminating the phenomenon of velocity separation. Figure 14 shows the velocity distribution of the flow field in the original and optimized models. In the original model, there is a clear separation of the velocity boundary layer on the upper and lower surfaces of the model. Because of this, there is an increase in the pressure difference between the upper and lower surfaces of the airframe, causing fluid disturbance around the airframe.

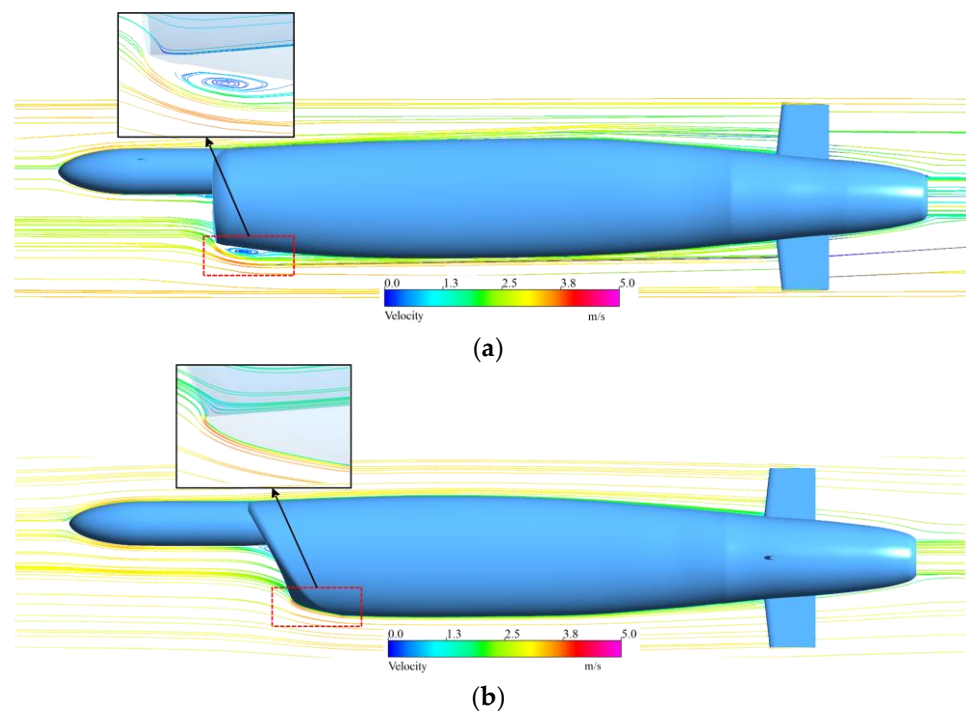


Figure 13. Streamline distribution. (a) Original modal and (b) optimized model.

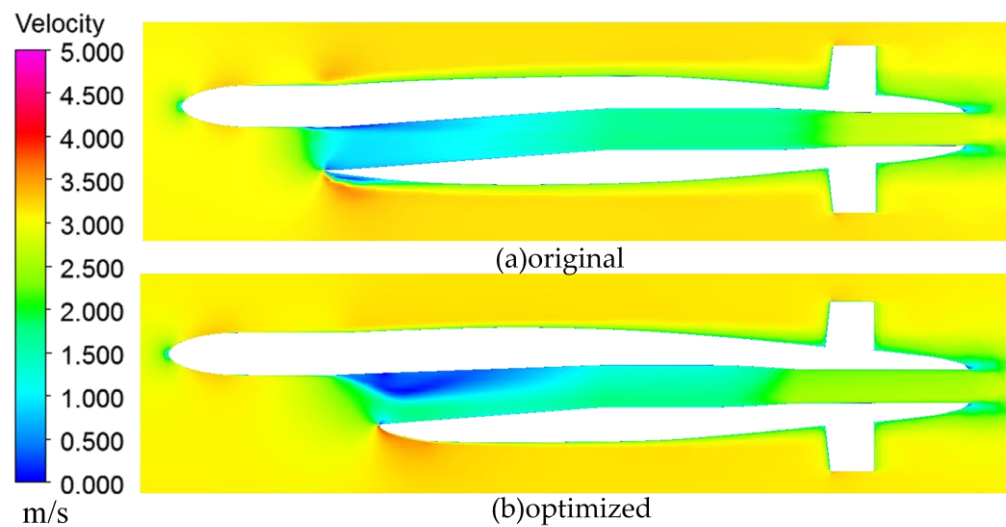


Figure 14. Velocity distribution.

The energy loss in the flow field can be analyzed indirectly through the velocity distribution in the flow field, but the exact value and location of the loss cannot be obtained directly. To address this issue, Kock [30] linked the entropy production based on the second law of thermodynamics with flow loss, analyzing entropy generation in an incompressible pipe flow and proposing an equation for calculating the turbulent pulsation entropy production. Through the entropy production calculation, the flow loss size and specific location can be intuitively expressed. Under adiabatic conditions, entropy production is composed of two parts: entropy production caused by time-averaged velocity and pulsation velocity, and entropy production caused by friction between the fluid and the wall. In flow fields solved by the Reynolds-averaged equations, the total entropy production is expressed as Equation (26).

$$S_{pro} = S_{pro,\bar{D}} + S_{pro,D'} + S_{pro,w} \tag{26}$$

where  $S_{pro,\bar{D}}$  is caused by time-averaged velocity,  $S_{pro,D'}$  is caused by pulsation velocity, and  $S_{pro,w}$  is caused by wall effect. The calculation formulas are expressed as follows:

- (1) Entropy production caused by time-averaged velocity:

$$S_{pro,\bar{D}} = \int_V S'''_{\bar{D}} dV \tag{27}$$

$$S'''_{\bar{D}} = \frac{\mu}{T} \left[ \left( \frac{\partial \bar{u}}{\partial y} + \frac{\partial \bar{v}}{\partial x} \right)^2 + \left( \frac{\partial \bar{u}}{\partial z} + \frac{\partial \bar{w}}{\partial x} \right)^2 + \left( \frac{\partial \bar{v}}{\partial z} + \frac{\partial \bar{w}}{\partial y} \right)^2 \right] \tag{28}$$

- (2) Entropy production caused by pulsation velocity:

$$S_{pro,D'} = \int_V S'''_{D'} dV \tag{29}$$

$$S'''_{D'} = \alpha \frac{\rho \omega k}{T} \tag{30}$$

- (3) Entropy production caused by the wall effect:

$$S_{pro,W} = \int_S \frac{\tau_w v_p}{T} dS \tag{31}$$

where  $\tau_w$  is the wall shear stress;  $v_p$  denotes the velocity vector at the center height of the first layer of the grid;  $\alpha$  is 0.09;  $\omega$  is the specific dissipation rate; and  $k$  is the turbulent kinetic energy.

Figure 15 shows the entropy production distribution of the AUV, which is consistent with the analysis of the velocity distribution, i.e., due to the boundary layer separation phenomenon, entropy production exists on the surface of the body, the back of the fin plate, and the exit of the flow channel in both models. The difference is that the entropy production of the original model is mainly concentrated at the inlet of the flow channel and the front of the bottom plate of the middle body. Significantly reduced energy losses are shown in the bottom plate of the middle body, while a small energy loss occurs at the flow channel inlet. In the original model, the sum of the total entropy production  $S_{pro}$  was 321 W/K. However, after optimization, the total entropy production decreased to 204 W/K, further confirming the effectiveness of the optimization.

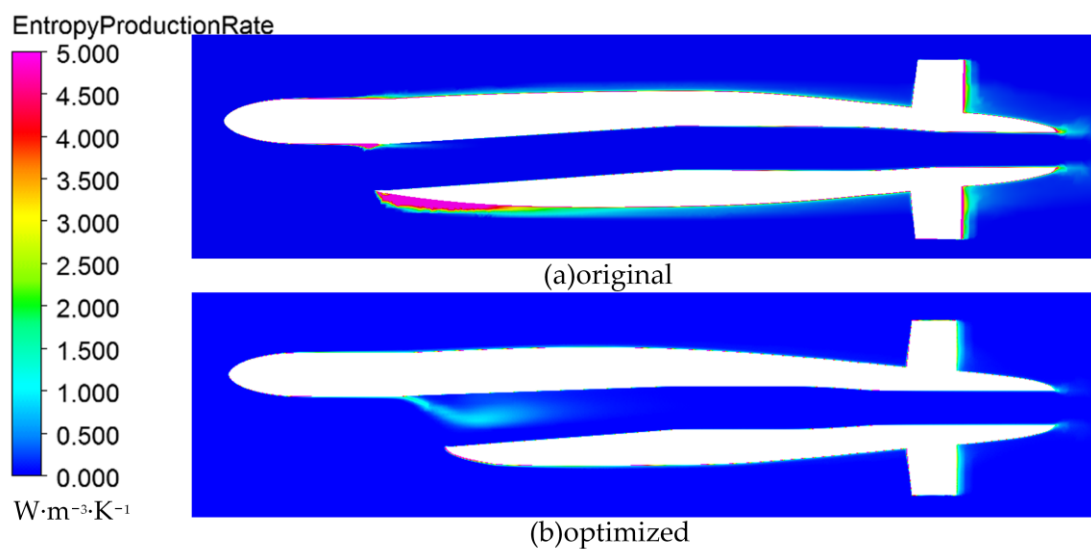


Figure 15. Distribution of entropy production.

## 5. Conclusions

In this paper, a bionic shark sailing body with an internal flow channel is proposed. The optimal design was carried out with the research objective of designing for low resistance, high discharge capacity, and low energy consumption. The analysis is concluded as follows:

- (1) The hydrodynamic numerical simulation method was determined with the process of computational domain generation, meshing, and CFD numerical simulation. The DARPA SUBOFF model was also validated.
- (2) The parametric modeling of an underwater vehicle inspired by the shape of a shark was achieved. Then, the design of the shape combination scheme was carried out by means of the optimal Latin hypercube method.
- (3) Surrogate models for the resistance, displacement volume, and energy consumption were constructed based on test samples. Then, the automatic optimization platform was built by Isight and the CFD simulation was replaced by the surrogate model. A multi-objective genetic algorithm was then used to solve the resistance, displacement volume, and energy consumption objective functions.
- (4) The model's streamlines, velocity distribution, and entropy production rate were analyzed, and it was observed that the separation of the boundary layer on the lower surface of the optimized model improved.

In this study, only variations in the AUV's shape were considered, without taking into account the effects of changes in the internal flow channels on resistance. Additionally, the influence of the accelerating flow from the propulsor on resistance was not considered.

In future work, variations in the flow channels and the impact of the propulsor will be taken into account, and the optimized model will be experimentally tested. In addition, the analysis of maneuverability and seakeeping will be added to the CFD to establish a mathematical model for a comprehensive hydrodynamic performance evaluation system.

**Author Contributions:** Conceptualization, Q.S. and J.Y.; methodology, Q.S.; software, Y.L.; validation, Y.L., J.L., and D.T.; formal analysis, Y.L.; investigation, Q.S.; resources, Y.L.; data curation, J.Y.; writing—original draft preparation, Y.L.; writing—review and editing, J.L.; visualization, D.T.; supervision, P.J.; project administration, Q.S.; and funding acquisition, P.J. All authors have read and agreed to the published version of the manuscript.

**Funding:** This work was supported by the National Natural Science Foundation of China (51976079), Special fund of technological innovation for carbon peak and carbon neutrality in Jiangsu Province (BE2022032-3), the Research Project of State Key Laboratory of Mechanical System and Vibration (MSV202201) and the Engineering Projects for Significant Scientific and Technological Achievements of Wuhu city (2022zc07).

**Institutional Review Board Statement:** Not applicable.

**Informed Consent Statement:** Not applicable.

**Data Availability Statement:** The data presented in this paper are available upon contacting the corresponding author.

**Acknowledgments:** The authors would like to thank the anonymous reviewers for their careful reading and valuable comments.

**Conflicts of Interest:** The authors declare no conflict of interest.

## References

- Zhao, Y.; Zeng, J.; Tan, Y. Neighborhood samples and surrogate assisted multi-objective evolutionary algorithm for expensive many-objective optimization problems. *Appl. Soft Comput.* **2021**, *105*, 107268.
- Li, X.; Lin, G. Study on multi-disciplinary design and multi-objective problem in conceptual design of AUV. *Ocean Technol.* **2008**, *27*, 77–82.
- Zhang, T.; Zhou, H.; Wang, J.; Liu, Z.; Xin, J.; Pang, Y. Optimum design of a small intelligent ocean exploration underwater vehicle. *Ocean Eng.* **2019**, *184*, 40–58. [[CrossRef](#)]
- Wu, H.; Niu, W.; Zhang, Y.; Wang, S.; Yan, S. A hybrid polynomial-based optimization method for underwater gliders with parameter uncertainty. *Appl. Ocean Res.* **2023**, *133*, 103486.
- Luo, W.; Lyu, W. An application of multidisciplinary design optimization to the hydrodynamic performances of underwater robots. *Ocean Eng.* **2015**, *104*, 686–697. [[CrossRef](#)]
- Bidoki, M.; Mortazavi, M.; Sabzehparvar, M. A new approach in system and tactic design optimization of an autonomous underwater vehicle by using multidisciplinary design optimization. *Ocean Eng.* **2018**, *147*, 517–530. [[CrossRef](#)]
- Tian, W.; Mao, Z.; Zhao, F.; Zhao, Z. Layout optimization of two autonomous underwater vehicles for drag reduction with a combined cfd and neural network method. *Complexity* **2017**, *2017*, 5769794. [[CrossRef](#)]
- Yan, Z.; Zhang, J.; Zeng, J.; Tang, J. Three-dimensional path planning for autonomous underwater vehicles based on a whale optimization algorithm. *Ocean Eng.* **2022**, *250*, 111070. [[CrossRef](#)]
- Fuglestad, A.L.; Grahl-Madsen, M. Computational Fluid Dynamics Applied on an Autonomous Underwater Vehicle. *ASME Int. Conf. Offshore Mech. Arct. Eng.* **2004**, *37459*, 447–451.
- Inoue, T.; Suzuki, H.; Kitamoto, R.; Watanabe, Y.; Yoshida, H. Hull form design of underwater vehicle applying CFD Computational Fluid Dynamics. In Proceedings of the Oceans'10 IEEE Sydney, Sydney, Australia, 24–27 May 2010; IEEE: New York, NY, USA, 2010; pp. 1–5.
- Safari, F.; Rafeeyan, M.; Danesh, M. Estimation of hydrodynamic coefficients and simplification of the depth model of an AUV using CFD and sensitivity analysis. *Ocean Eng.* **2022**, *263*, 112369. [[CrossRef](#)]
- Jin, X.; Yang, S.; Chen, H. Research on fairing design and cfd analysis of submarine pipeline inspection arv. *MATEC Web Conf.* **2017**, *108*, 07003. [[CrossRef](#)]
- Sener, M.Z.; Aksu, E. The effects of head form on resistance performance and flow characteristics for a streamlined AUV hull design. *Ocean Eng.* **2022**, *257*, 111630.
- Jouhaud, J.-C.; Sagaut, P.; Montagnac, M.; Laurencea, J. A surrogate-model based multidisciplinary shape optimization method with application to a 2d subsonic airfoil. *Comput. Fluids* **2007**, *36*, 520–529. [[CrossRef](#)]
- Luo, W.; Guo, X.; Dai, J.; Rao, T. Hull optimization of an underwater vehicle based on dynamic surrogate model. *Ocean Eng.* **2021**, *230*, 109050. [[CrossRef](#)]

16. Hu, F.; Huang, Y.; Xie, Z.; Yu, J.; Wang, Z.; Qiao, J. Conceptual design of a long-range autonomous underwater vehicle based on multidisciplinary optimization framework. *Ocean Eng.* **2022**, *248*, 110684. [[CrossRef](#)]
17. Raayai-Ardakani, S.; McKinley, G.H. Geometric optimization of riblet-textured surfaces for drag reduction in laminar boundary layer flows. *Phys. Fluids* **2019**, *31*, 053601.
18. Wang, Y.; Wang, Z.; Li, J. Initial Design of a Biomimetic Cuttlefish Robot Actuated by SMA Wires. In Proceedings of the 2011 Third International Conference on Measuring Technology and Mechatronics Automation, Shanghai, China, 6–7 June 2011; pp. 425–428.
19. Xu, H.; Pan, C.; Xie, H.; Zhang, D. Dynamics modeling and simulation of a bionic swim bladder system in underwater robotics. *J. Bionic Eng.* **2008**, *5*, 66–71. [[CrossRef](#)]
20. Pena, B.; Huang, L. A review on the turbulence modelling strategy for ship hydrodynamic simulations. *Ocean Eng.* **2021**, *241*, 110082.
21. Huang, L.; Tavakoli, S.; Li, M.; Dolatshah, A.; Pena, B.; Ding, B.; Dashtimanesh, A. CFD analyses on the water entry process of a freefall lifeboat. *Ocean Eng.* **2021**, *232*, 109115. [[CrossRef](#)]
22. Won, D.; Kim, J.; Kim, J. Design optimization of duct-type AUVs using CFD analysis. *Intel. Serv. Robot.* **2015**, *8*, 233–245. [[CrossRef](#)]
23. Hu, R.; Liu, D.; Wang, S. Research on the numerical simulation of cavity for one projectile underwater. *Ship Sci. Technol.* **2021**, *43*, 38–40.
24. Liu, H.; Huang, T. *Summary of DARPA Suboff Experimental Program Data*; Naval Surface Warfare Center, Carderock Division (NEWCCD): Bethesda, MD, USA, 1998.
25. Song, B.; Pan, G.; Zhang, L.; Huang, Q.; Yu, Y.; Tian, W. Development trend and key technologies of autonomous underwater vehicles. *Chin. J. Ship Res.* **2022**, *17*, 27–44.
26. Jiang, X.; Liu, Y. Installation Structure Optimization and Vortex Noise Analysis for Appendages of Deepwater AUV. *J. Mech. Eng.* **2015**, *51*, 25–34. [[CrossRef](#)]
27. Schmit, L.; Farshi, B. Some Approximation Concepts for Structural Synthesis. *AIAA J.* **1974**, *12*, 692–699. [[CrossRef](#)]
28. Wu, Z. Radial basis function scattered data interpolation and the meshless method of numerical solution of PDEs. *Chin. J. Eng. Math.* **2002**, *19*, 1–12.
29. Song, B.; Du, W.; Gao, Z.; Cai, W.; Wen, Z. Multidisciplinary Design Optimization of Torpedo General Design Based on Collaborative Optimization. *Torpedo Technol.* **2009**, *17*, 7–11.
30. Kock, F.; Herwig, H. Local entropy production in turbulent shear flows: A high-reynolds number model with wall functions. *Int. J. Heat Mass Transf.* **2004**, *47*, 2205–2215. [[CrossRef](#)]

**Disclaimer/Publisher’s Note:** The statements, opinions and data contained in all publications are solely those of the individual author(s) and contributor(s) and not of MDPI and/or the editor(s). MDPI and/or the editor(s) disclaim responsibility for any injury to people or property resulting from any ideas, methods, instructions or products referred to in the content.